IAHR AIRH

4-th International Meeting on
Cavitation and Dynamic Problems in Hydraulic Machinery and Systems,
October, 26-28, 2011, Belgrade, Serbia

Influence of the Pump-Turbine Guide Vanes Vibrations on the Pressure Fluctuations in the Rotor-Stator Vaneless Gap

Steven Roth, Vlad Hasmatuchi, Francisco Botero, Mohamed Farhat, François Avellan

EPFL, Laboratory for Hydraulic Machines
33bis Av. de Cour, Lausanne, 1007, Switzerland, steven.roth@epfl.ch, vlad.hasmatuchi@epfl.ch,
francisco.botero@epfl.ch, mohamed.farhat@epfl.ch, francois.avellan@epfl.ch

Abstract

We investigate the Rotor-Stator Interaction in a pump-turbine reduced scale model by considering fluid-structure coupling. The pressure fluctuations amplitude in the rotor-stator vaneless gap has generally been shown to increase linearly with the operating specific energy, subjecting the pump-turbines components to high stresses at high head operations. However, the present paper shows that the guide vanes vibratory properties may have a strong influence on the amplitude of the pressure fluctuations which are due to the Rotor-Stator Interaction. Thus, their amplitude may locally drop by 50% close to guide vanes reaching resonance.

Keywords: Hydraulic machines, pump-turbines, fluid-structure coupling, rotor-stator interaction, guide vanes cascade, wicket gates cascade.

1. Introduction

Pumped-storage power plants go hand in hand with new renewable CO_2-free energies. They also ensure a safe country wide supply of electricity. Cracks, or even failures, may appear in pump-turbines components [1], [2]. The reliability and safety of pump-turbines tend, thus, to be ensured at all levels aiming to reduce the maintenance costs. In particular, guide vanes may experience strong vibrations [3]. Recently, Nennemann et al. [4] simulate numerically complex guide vanes vibrations phenomena experienced by the YiXing pump-turbines. High cycle fatigue strength may lead to the propagation of cracks and the failure of shear pin [5] or guide vanes stem [6]. The damage root causes can range from the misalignment during shear pins assembly on the guide vane activation mechanism, causing anomalous loading [5], to the strong excitation due to the Rotor-Stator Interaction, RSI, [7], [8] and [9].

Within the framework of the HYDRODYNA research project, we focus our investigation on the RSI excitation source and the consequences on the guide vanes cascade vibrations by considering the fluid-structure coupling. In [10], we already describe the advanced instrumentation used in a pump-turbine reduced scale model for investigating fluid-structure coupling. In [11], we highlight the interaction between the vibrating structures and the surrounding flow in the guide vanes cascade.

The present work describes the guide vanes vibratory properties influence on the pressure fluctuations in the rotor-stator vaneless gap due to RSI, in a pump-turbine reduced scale model. The guide vanes vibrations and the pressure fluctuations are monitored while the pump-turbine is operated at different rotating speeds. The specific energy and the discharge are adjusted in order to keep the pump-turbine model at the Best Efficiency operating Point, BEP, conditions. We focus our attention on the main RSI modes.

How is the guide vanes modal behavior influenced by the surrounding flow? How are the guide vanes vibrations retrospectively influencing the pressure field in the rotor-stator vaneless gap? These are the questions which are addressed in the paper

The paper starts by presenting the RSI case study. Next, the test rig as well as the specific instrument set used to monitor the fluid-structure coupling is described. Then, prior to the results presentation, the testing conditions are given. Finally, a discussion concludes the paper.

2. RSI case study

The investigation of the RSI influence on the vibrations of the guide vanes are performed with the low specific speed $\nu = 0.17$ [12] HYDRODYNA pump-turbine reduced scale model featuring $z_b = 9$ impeller blades and $z_o = 20$ guide vanes.

The relative efficiency η/η_{max} hill chart in turbine mode for guide vanes opening angles α_o ranging from 12° to 34° is given in Fig. 1.

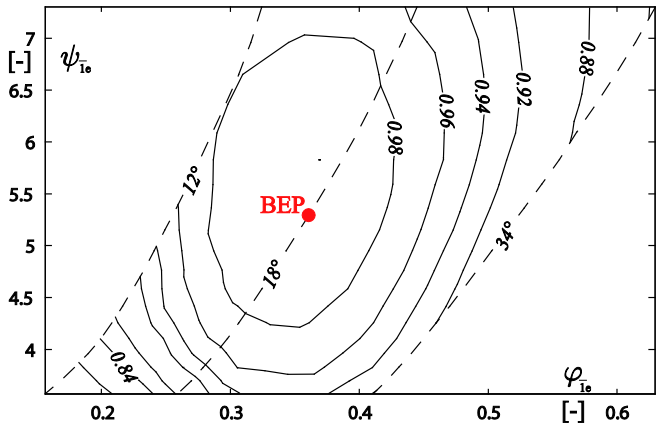

Fig. 1 Relative efficiency η/η_{max} hill chart in generating mode for opening angles α_o ranging from 12° to 34°

The pressure field in the rotor-stator vaneless gap resulting from the RSI may be expressed as the superposition of the components p_k of each diametrical mode k, see [7]:

$$p(t,\theta_s) = \sum_k^{\infty} p_k(t,\theta_s) = \sum_k^{\infty} A_k \left[\sin(2\pi m z_b n \cdot t) \cdot \cos(k\theta_s + \phi_k)\right] \tag{1}$$

with $k = mz_b \pm m'z_o$ being the number of diametrical nodes, and θ_s, the angular position in the stator.

The interaction $z_b = 9$ impeller blades and $z_o = 20$ guide vanes make apparent the main RSI diametrical modes $k = -11$ and $k = -2$, with the corresponding values of the mode rotating frequency $f = mz_b n$, see Table 1.

Table 1 Main RSI modes for a pump-turbine featuring $z_b = 9$ impeller blades and $z_o = 20$ guide vanes with the frequency f given as a multiple of the impeller frequency n

m	m'	k	f
1	1	-11	$9n$
2	1	-2	$18n$

In Fig. 2, the phase average of typical pressure fluctuations in the vaneless gap is shown on the left hand side, against the number of impeller revolutions. On the right hand side, the phase average of typical guide vanes vibrations is given. The two modes $k = -11$ and $k = -2$, rotating at $9n$ and $18n$, respectively, in the opposite direction than the impeller rotation, predominate in both the pressure fluctuations and the structural vibrations signals.

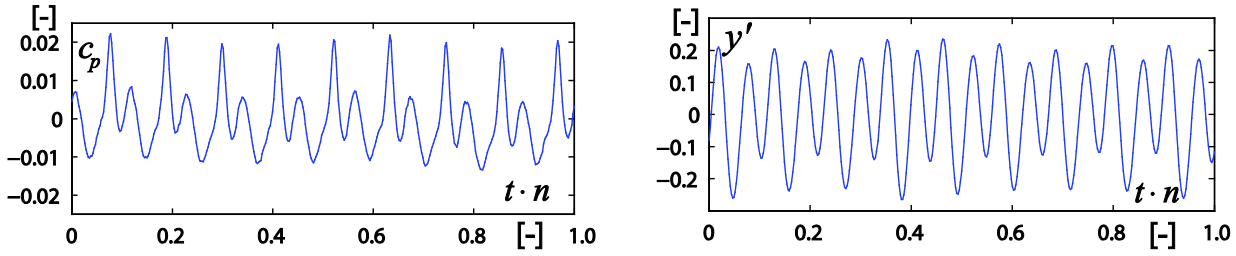

Fig. 2 Phase average of typical pressure fluctuations in the vaneless gap, on the left hand side, and guide vanes vibrations, on the right hand side, against the number of impeller revolutions

3. Experimental setup

The HYDRODYNA pump-turbine reduced scale model, whose reference diameter, $D_{\bar{1}e}$, is 0.250 m, is installed on the EPFL PF2 test rig, see Fig. 3, featuring a maximum discharge $Q = 1.4\ \mathrm{m^3/s}$ and a maximum specific energy $E = 1'150\ \mathrm{J/kg}$; the maximum rotation speed being limited to $N = 2'500\ \mathrm{rpm}$.

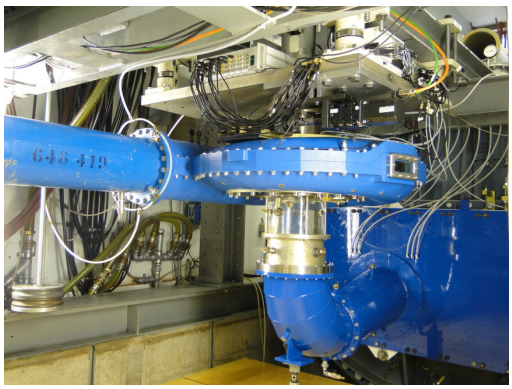

Fig. 3 Hydrodyna reduced scale model installed on the EPFL PF2 test rig

Usually, the 20 guide vanes of the cascade have stiff stem to ensure not to exceed the material yield strength. In our investigation, two guide vanes, o_{10} and o_{11}, have flexible stem. They are placed adjacently in the cascade at the angular positions θ_{o10} and θ_{o11} in between stiff guide vanes, see Fig. 4. The flexible stem, see Fig. 5, enables to emphasize the fluid-structure coupling by increasing the vibrations amplitude. The frequency of the first bending eigen mode is 232 Hz for both guide vanes in water, model at rest.

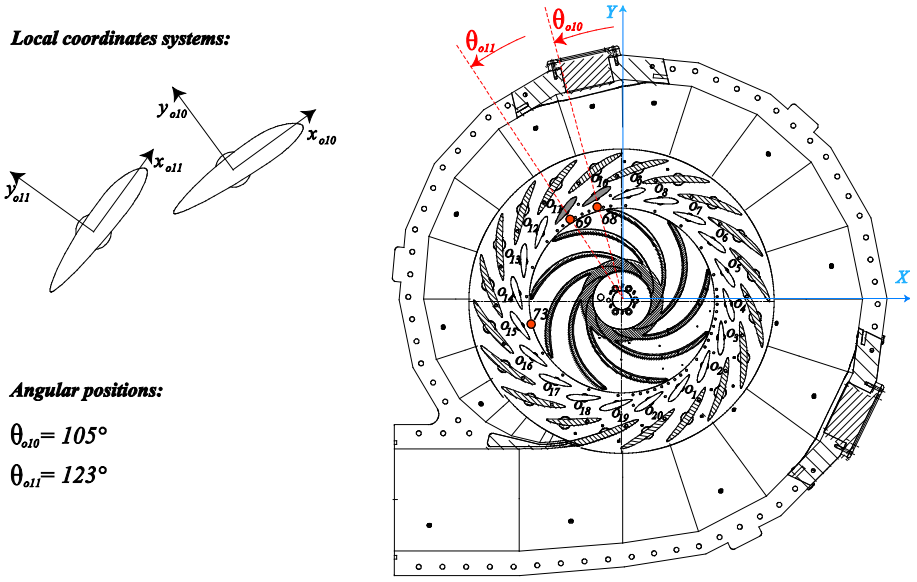

Fig. 4 Flexible guide vanes and pressure sensors location in the cascade

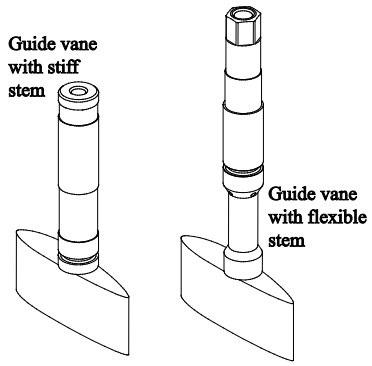

Fig. 5 Guide vane with stiff and flexible stem

The guide vanes, o_{10} and o_{11}, are instrumented with full Wheatstone piezo-resistive strain gages bridges [10]. The locations of the strain gages as well as their characteristics are shown in Fig. 6.

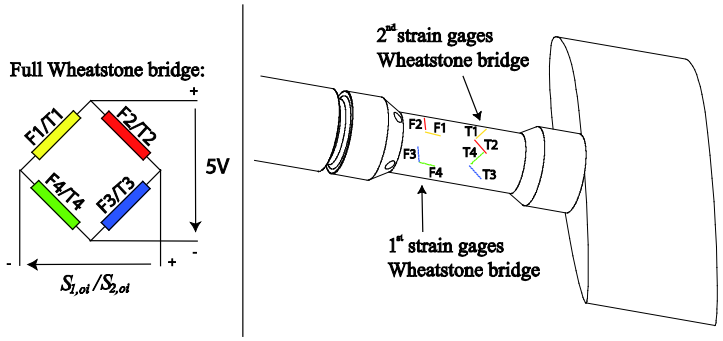

Strain gages characteristics:	
Gage length	2 mm
Gage resistance	120 Ω
Gage factor	100
Max. allowable strain	3'000 μm/m
Max. allowable current	20 mA

Calibration coefficients:

a_{oi0} = -195.5 N/V

b_{oi0} = -41.7 N/V

a_{oi1} = -178.7 N/V

b_{oi1} = -15.7 N/V

Fig. 6 Location and characteristics of strain gages, and guide vanes calibration coefficients

The instrumented guide vanes, o_{10} and o_{11}, are statically calibrated by applying a pure bending force F_{oi}, defined in the same direction as y_{oi}, see Fig. 4. To have a complete description of the calibration setup, the reader is kindly asked to refer to [10]. Subjecting the guide vanes to thirty-nine different bending force values obtained with weights up to 15.2 kg, corresponding to force values ranging from -149.1 N to 149.1 N, the two static calibration coefficients a_{oi} and b_{oi} relating the static force to the two Wheatstone bridges voltage output, $S_{1,oi}$ and $S_{2,oi}$ are estimated, by using a multivariate linear regression, see Fig. 6. The absolute uncertainty is in the range ±1.4 N and ±2.4 N for o_{10} and o_{11}, respectively. The static force applied on the guide vane o_i is given by:

$$F_{oi} = a_{oi} \cdot S_{1,oi} + b_{oi} \cdot S_{2,oi} \tag{2}$$

Three miniature piezo-resistive pressure sensors [13] are flush mounted at the wall of the headcover in the rotor-stator vaneless gap, see Fig. 4. The pressure sensors 68 and 69 are located close to the guide vane o_{10} and o_{11}, respectively, whereas the pressure sensor 73 is positioned far from the guide vanes with flexible stem. The pressure sensors are calibrated statically up to 0.6 MPa absolute pressure, with 50 intermediate points. The characteristics of the pressure sensors are given in Table 2.

Table 2 Pressure sensors characteristics

Characteristics	Value
Measurement range	0÷0.6 MPa
Abs. Measurement uncertainty	±0.4 kPa
Sensitivity	70.5 kPa/V
Sensitive area	∅ 1mm
Bandwidth	0÷25 kHz

The pressure fluctuations as well as the guide vanes vibrations signals are simultaneously recorded with NI PXI 4472B digitizers with 24 bits A/D resolution at 5 kHz sampling frequency over 15.36 s.

4. Testing conditions

The guide vanes forced response is measured over a wide frequency range by varying the main RSI frequency. We focus the experimental investigation on the Best Efficiency operating Point, BEP, in turbine mode, corresponding to $\alpha_o = 18°$ guide vanes opening angle, a discharge coefficient φ_{1e}=0.36 and a specific energy coefficient ψ_{1e}=5.3, [12], see Fig. 1. The impeller rotating speed N is varied from 700 min^{-1} to 910 min^{-1}, corresponding to an impeller frequency n ranging from 11.67 Hz to 15.17 Hz. The specific energy E and the discharge Q are adjusted to keep the pump-turbine model at the BEP operating conditions. The guide vanes vibrations and the pressure fluctuations are thereby monitored while the RSI 1st harmonic frequency, one of the main RSI mode frequency, ranging from 210 Hz to 273 Hz, cross the 1st bending eigen frequencies of the guide vanes, 232 Hz.

In Fig. 7, the experimental values of the specific energy and the discharge used to maintain the operating conditions at the BEP are plotted against the impeller frequency n. The experimental values of the specific energy E_{exp} range from 223.6 J/kg to 372.4 J/kg and those of the discharge Q_{exp} range from 0.162 m^3/s to 0.211 m^3/s. In addition, the figure gives the value of the specific energy E and discharge Q that would have been obtained if we would have reached the exact value of φ_{1e} and ψ_{1e}. With the relative differences $\delta_{\varphi_{1e}}$ and $\delta_{\psi_{1e}}$, also plotted in Fig. 7, we illustrate the offset between experimental and expected values of the coefficients, which is less than 1% for all investigated impeller frequencies n.

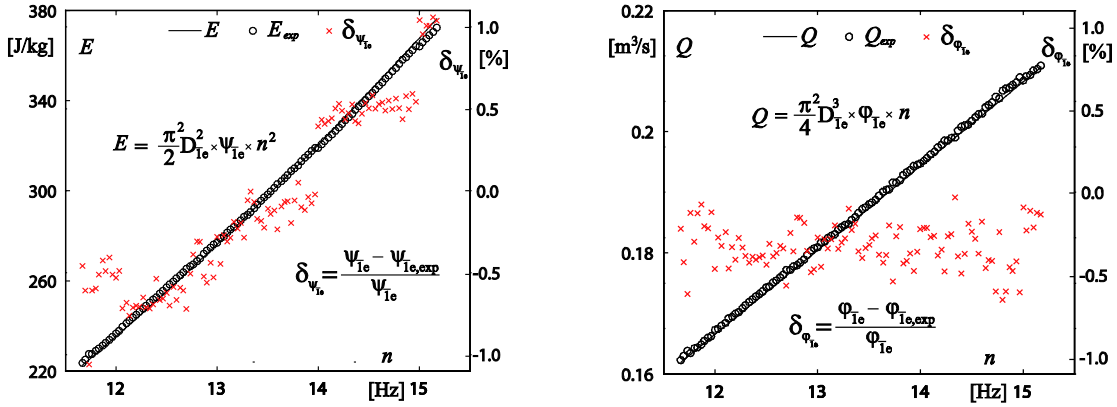

Fig. 7 Experimental and expected values of specific energy, E_{exp} and E, and discharge, Q_{exp} and Q, versus impeller frequency n to ensure the BEP operating conditions

5. Results

The values of both the guide vanes vibrations and the pressure fluctuations in the vaneless gap are made non dimensional by introducing the relative fluctuating bending displacement and the pressure fluctuations factor.

The relative fluctuating bending displacement y'_{oi} of the i^{th} guide vane is defined as follows:

$$y'_{oi}(t) = \frac{y_{oi}(t) - \bar{y}_{oi}}{\bar{y}_{oi}}, \text{ for } 1 \le i \le z_o \tag{3}$$

where y_{oi} and $\bar{y}_{oi}$ are the i^{th} guide vane bending displacement and its time average, respectively.

Moreover, the stiffness value of the non-instrumented guide vanes being much higher than the stiffness of instrumented guide vanes, we can neglect the vibrations of these guide vanes, yielding :

$$y'_{oi}(t) = 0, \text{ for } (1 \le i \le 9) \cup (12 \le i \le z_o) \tag{4}$$

The bending stiffness coefficient c_i is defined as:

$$F_{oi} = c_i \cdot y_{oi}, \text{ for } i = 10,\ 11 \tag{5}$$

By substituting eq. (5) in eq. (2), the relative fluctuating displacement is recovered directly from the output voltage signals which yields

$$y'_{oi} = \frac{y_{oi} - \bar{y}_{oi}}{\bar{y}_{oi}} = \frac{a_{oi}\left(S_{1,oi} - \bar{S}_{1,oi}\right) + b_{oi}\left(S_{2,oi} - \bar{S}_{2,oi}\right)}{a_{oi}\bar{S}_{1,oi} + b_{oi}\bar{S}_{2,oi}}, \text{ for } i = 10,11 \tag{6}$$

The pressure fluctuations factor c_p is defined as follows:

$$c_p = \frac{p - \bar{p}}{\rho \cdot E} \tag{7}$$

where ρ is the water density, E, the specific energy of the pump-turbine related to the operating point, p, the pressure and, finally, $\bar{p}$, the pressure time average.

The RMS-values of the pressure fluctuations factor $\tilde{c}_p$ for the pressure sensors 68, 69 and 73 are plotted against the RSI 1st harmonic frequency in the left hand side of Fig. 8, while the RMS-values of the relative fluctuating displacement $\widetilde{y'}_{oi}$ of the guide vanes o_{10} and o_{11} are plotted in the right hand side.

The pressure sensor 73 exhibits a fairly constant RMS-value around $\tilde{c}_{p,73} = 0.0098$ while the pressure sensors 68 and 69, located close to the guide vanes o_{10} and o_{11}, respectively, experience non-constant RMS-values; After a maximum reached at 225 Hz, the RMS-value is decreasing. The relative difference between the maximum and the minimum RMS-values $\tilde{c}_p$ for the pressure sensors 68 and 69 is 50% and 30%, respectively. Thereby, a transfer of energy should occur locally from the flow to the vibrating guide vanes, o_{10} and o_{11}, located close to the pressure sensors 68 and 69, respectively.

The guide vane o_{10} experiences indeed a maximum RMS-value $\widetilde{y'}_{o10}$ at 233 Hz, which is close to the 1st bending eigen frequency, 232 Hz, in water, model at rest. As for the guide vane o_{11}, its RMS-value $\widetilde{y'}_{o11}$ presents a maximum at 225 Hz and a minimum at 233 Hz. Therefore, this guide vane does not respond preferably at the 1st bending eigen frequency in water, model at rest, but at a 3% lower frequency. The phase shift between the guide vane o_{10} excitation and the one of the guide vane o_{11} prevents the two guide vanes to vibrate preferably at the same frequency. These two frequencies, 225 Hz and 233 Hz, may nevertheless be considered as the eigen frequencies of the guide vanes cascade excited with the RSI.

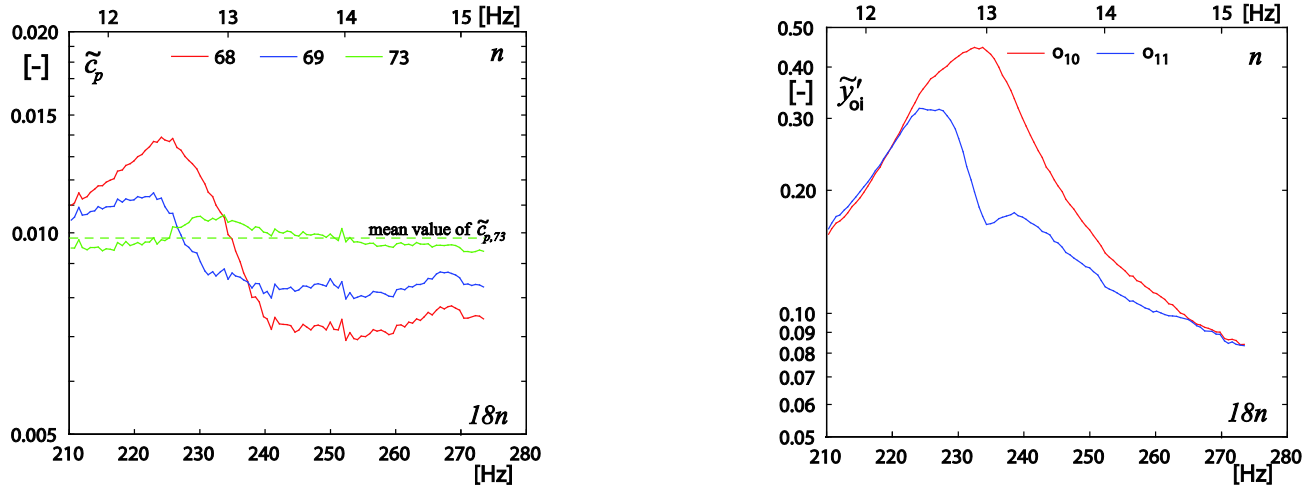

Fig. 8 RMS-value of the pressure fluctuations factor, left, for the pressure sensors 68, 69 and 73, and of the relative fluctuating displacement of the guide vane vanes o_{10} and o_{11}, right, against RSI 1st harmonic frequency for each impeller frequency

The pressure fluctuations close to the vibrating guide vanes seem, thereby, to be strongly influenced by their vibrations. Therefore we have computed the pressure fluctuations factor $\overline{P_{c_p c_p}}$ and relative fluctuating displacement $\overline{P_{y'y'}}$ power spectral densities to have a better understanding of the phenomenon.

We introduce $x_k(t)$ and $x_l(t)$ as either a pressure fluctuations factor or a relative fluctuating bending displacement signal. The signal $x_k(t)$ of total time signal length M_t is divided into $n_d = 8$ segments each of time signal length M, which overlap at 50%. The Fourier transforms of the segmented signals are obtained after subtracting the time average and after applying the Hanning windowing function. The Fourier transforms are denoted by $X_{k,m}(f)$ and $X_{l,m}(f)$, respectively.

The power spectral density estimate of the signal $x_k(t)$ is then defined as:

$$\overline{P_{x_k x_k}}(f_i) = \frac{1}{n_d}\sum_{m=1}^{n_d} X^*_{k,m}(f_i) X_{k,m}(f_i) \tag{8}$$

The phase shift $\phi_{k,l}$ between $X_{k,m}(f_i)$ and $X_{l,m}(f_i)$ at the frequency f_i is computed by taking the argument of the cross power spectral density estimate of the signals $x_k(t)$ and $x_l(t)$:

$$\phi_{k,l}(f_i) = \arg\left(\overline{P_{x_k x_l}}(f_i)\right) = \arg\left(\frac{1}{n_d}\sum_{m=1}^{n_d} X^*_{k,m}(f_i) X_{l,m}(f_i)\right) \tag{9}$$

The waterfall diagrams of the power spectral densities amplitude of the pressure fluctuations factor monitored with the pressure sensors 73, 68 and 69 are presented for the whole range of impeller frequencies n, in Fig. 9, Fig. 10 and Fig. 11, respectively. The left hand side of the figures represents the waterfall spectra as a 3D surface, whereas the right hand side is a contour plot. The frequency axis is made dimensionless with the impeller frequency n to highlight the RSI fundamental and its harmonics with the multiples of the impeller blades number mz_b.

Most of the spectral energy is concentrated at frequencies $f = mz_b n$, revealing the RSI modes. However, the two main RSI modes, rotating at $-9n$ and $-18n$, present, as expected, higher amplitude than the modes at higher $f/n = mz_b$ ratios. In Fig. 9 and Fig. 10, the spectra amplitude at $f/n = 18$ for the pressure sensor 68 and 69, respectively, varies strongly depending on the impeller frequency n. For impeller frequencies n ranging from 12.78 Hz to 15.17 Hz, the spectra amplitude at the RSI fundamental frequency strongly dominates the one at the RSI 1st harmonic. In contour plots, the neighboring guide vane 1st bending eigen mode influence on the pressure fluctuations may be observed. A small fraction of the spectral energy is indeed distributed around this structural eigen mode frequency. Owing to the axis normalization with varying impeller frequency n, this spectral energy concentration appears

obliquely in the waterfall spectra contour plot. In Fig. 11, since the guide vanes neighboring the pressure sensor 73 have stiff stem, no influence of structural vibrations are observed, and, thus, the spectra amplitude at $f = 18n$ remains constant with increasing impeller frequency n.

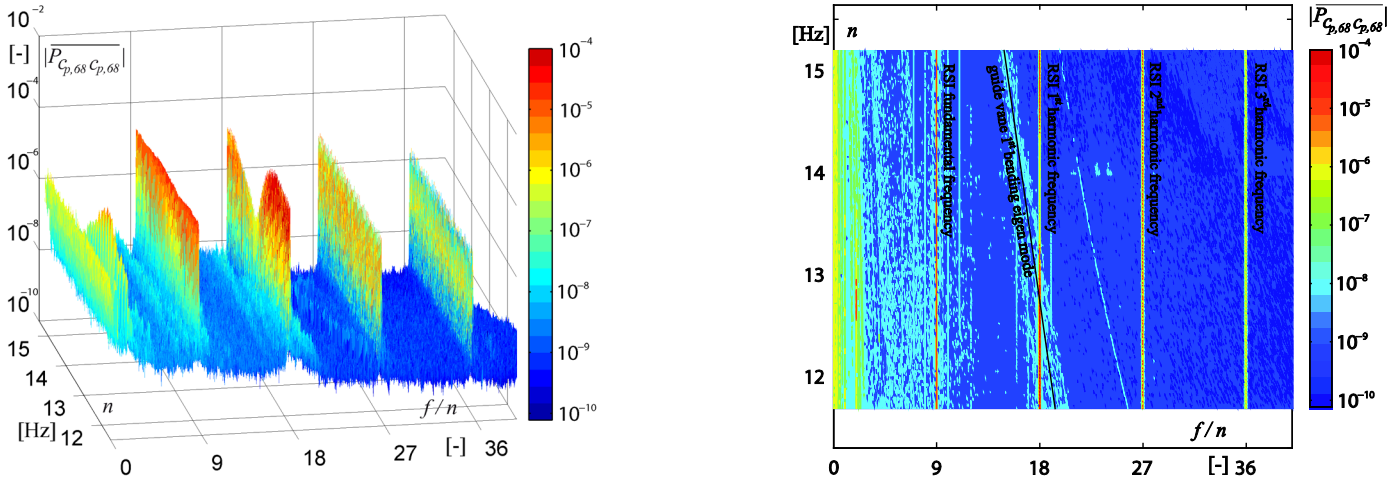

Fig. 9 Waterfall diagram of power spectral densities amplitude of the pressure fluctuations factor monitored with the pressure sensor 68, against the different impeller frequencies n

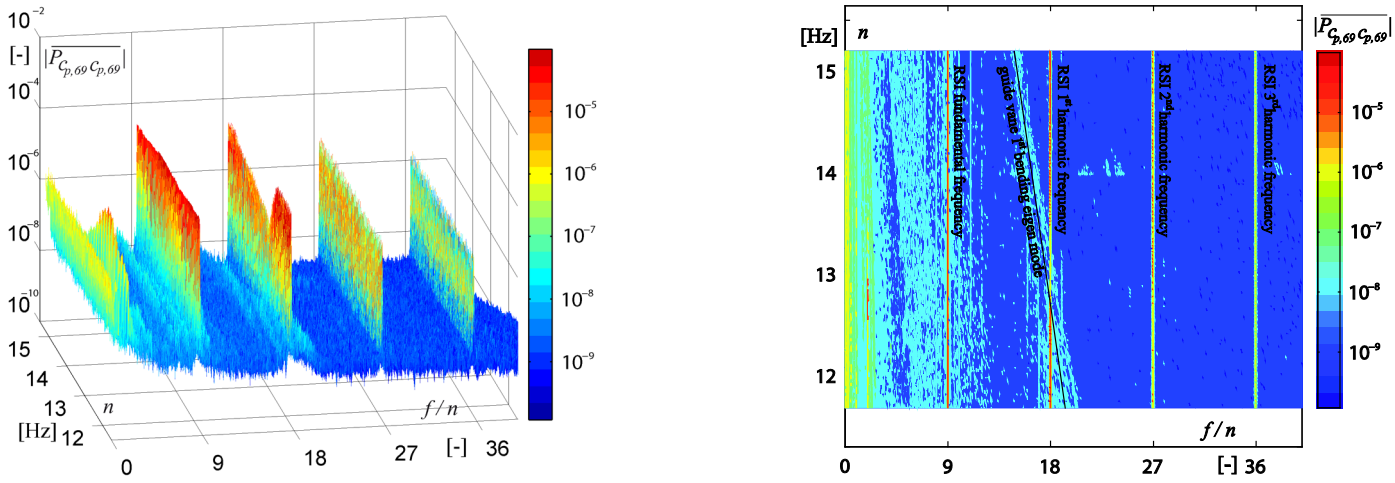

Fig. 10 Waterfall diagram of power spectral densities amplitude of the pressure fluctuations factor monitored with the pressure sensor 69, against the different impeller frequencies n

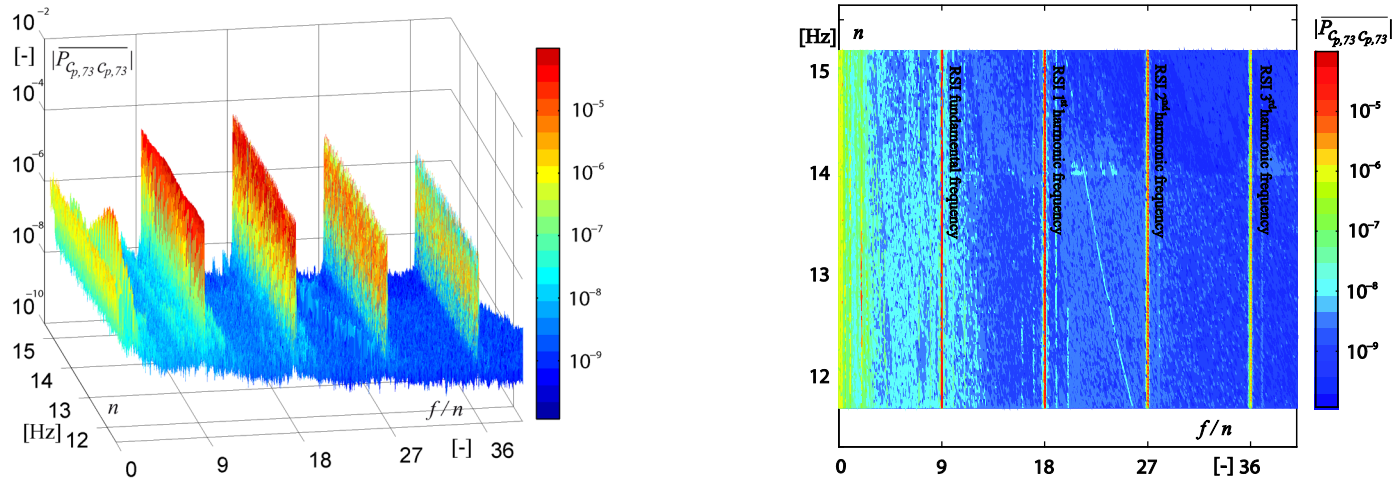

Fig. 11 Waterfall diagram of power spectral densities amplitude of the pressure fluctuations factor monitored with the pressure sensor 73, against the different impeller frequencies n

The waterfall diagrams of the power spectral densities amplitude of the relative fluctuating displacement for the guide vane o_{10} and o_{11} are presented for the whole range of impeller frequencies n, in Fig. 12 and Fig. 13, respectively. Similarly to the figures related to the pressure fluctuations factor, the left hand side of the figures represents the waterfall spectra as a 3D surface, whereas the right hand side is a contour plot.

Due to the RSI excitation, made of the superposition of rotating diametrical modes, most of the spectral energy is concentrated at RSI modes frequencies $f = mz_b n$. The response of the guide vanes to the two main RSI modes is the highest. The 1st bending eigen mode is now clearly observed in the contour plots of the relative fluctuating displacement power spectral densities amplitude. The guide vane 1st bending eigen frequency cross indeed the RSI 1st harmonic frequency. When the RSI 1st harmonic frequency approaches the 1st bending eigen mode frequency, the guide vanes response to this frequency is amplified. The response of the guide vanes to the RSI 1st harmonic depends, thus, on the impeller frequency n, due to their 1st bending eigen mode.

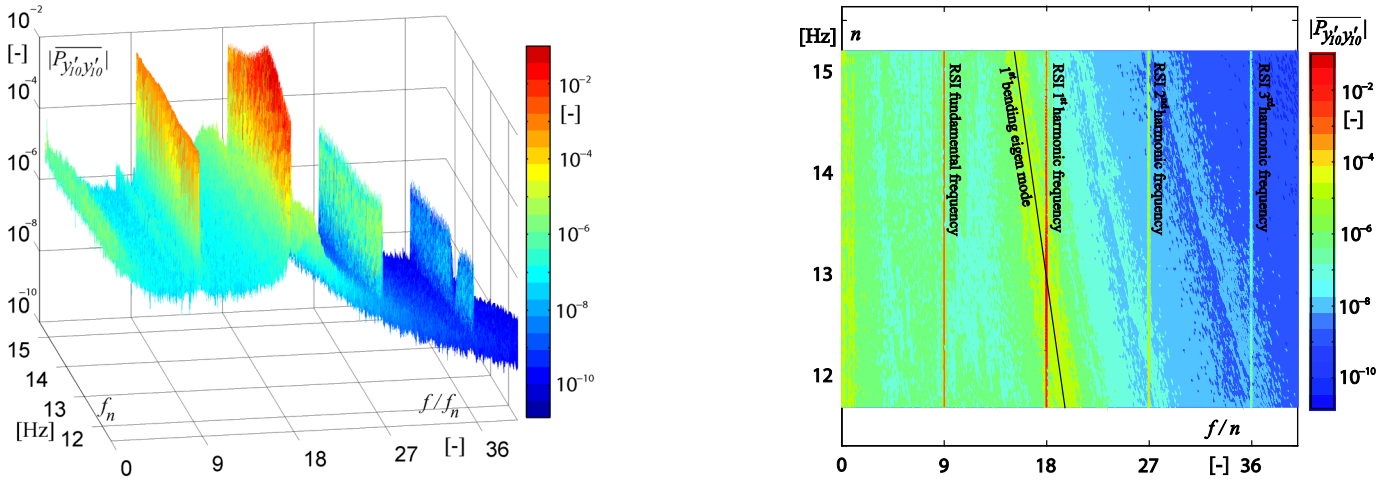

Fig. 12 Waterfall diagram of the power spectral density amplitude of the guide vanes o_{10} relative fluctuating displacement, against the different impeller frequencies n

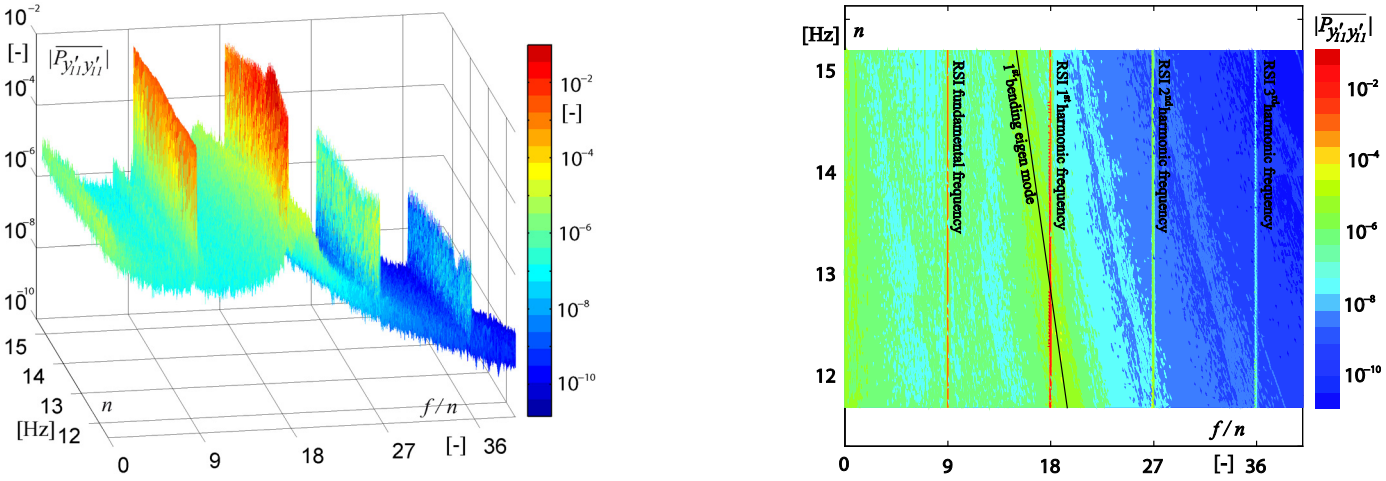

Fig. 13 Waterfall diagram of the power spectral density amplitude of the guide vanes o_{11} relative fluctuating displacement, against the different impeller frequencies n

As spectra amplitude only varies at the RSI 1st harmonic frequency according to different impeller frequencies n, we focus our attention on this frequency from now on. The pressure fluctuations factor $|\overline{Pc_p c_p}|$ and relative fluctuating displacement $|\overline{P_{y'y'}}|$ power spectral densities amplitude at the RSI 1st harmonic frequency are plotted against the RSI 1st harmonic frequency $18n$ for the whole range of impeller frequency n investigated on the left and right sides of Fig. 14, respectively.

As already mentioned, the spectra amplitude at the RSI 1st harmonic does not vary with increasing impeller frequency n for the pressure sensor 73. In the contrary, the spectra amplitude for the pressure sensors 68 and 69 starts to decrease at frequencies above 225 Hz, which corresponds to the frequency at which the guide vane o_{11} sees its amplitude diminishing. The minimum is observed at 243 Hz and 231 Hz for the pressure sensor 68 and 69, respectively. These frequencies are up to 5% higher than those at which the guide vanes are responding preferably, 233 Hz and 225 Hz. The ratio between the maximal and minimal pressure fluctuations amplitude is 12 for the pressure sensor 68 and 4 for the pressure sensor 69.

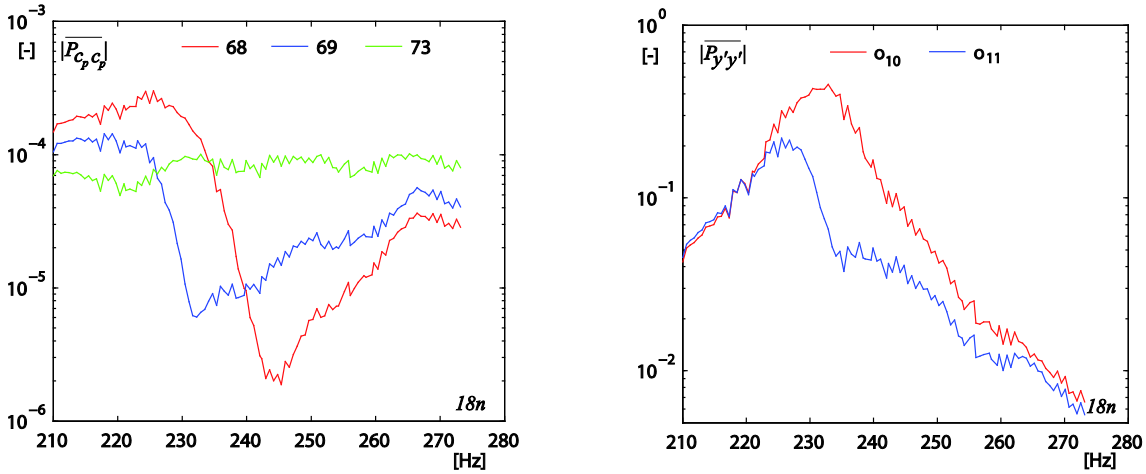

Fig. 14 Pressure fluctuations factor and guide vanes relative fluctuating displacement power spectral density amplitude for the pressure sensors 68, 69 and 73 vs. the RSI 1st harmonic frequency at different rotating speeds

The phase shift $\phi_{10,11}$ between the relative fluctuating displacement of the guide vanes o_{10} and o_{11} and the related group delay τ_g are plotted against the RSI 1st harmonic frequency $18n$ for the whole range of impeller frequency n investigated, in Fig. 15.

The phase is computed by taking the argument of the cross power spectral density estimate of $y'_{o10}(t)$ and $y'_{o11}(t)$, as shown in eq. (9). The group delay is defined as the negative of the rate of change of phase with frequency:

$$\tau_g(f) = -\frac{\partial(\phi(f))}{\partial f} \tag{10}$$

At the guide vanes cascade eigen frequencies, 225 Hz and 233 Hz, the group delay τ_g between the two guide vanes bending motions presents extrema, as stated by structural vibrations theory [14].

Consequently, between these two extrema of τ_g, at 231 Hz, the phase shift $\phi_{10,11}$ reaches a maximum. This frequency corresponds to the frequency at which the pressure fluctuations monitored with the pressure sensor 69 are minimal. Then, the phase shift $\phi_{10,11}$ presents a minimum at 243 Hz, which is the frequency at which the pressure sensor 68 monitors minimum pressure fluctuations. At 231 Hz and 243 Hz, the phase shift is the farthest from the phase shift monitored far from resonance, at 210Hz : $\phi_{10,11}(f = 210Hz) = 0.47rad$. As a result, the pressure fluctuations in the rotor-stator vaneless gap are minimal when the phase shift between guide vanes vibrations is the farthest from the phase shift, only due to the blade passage, observed out of resonance.

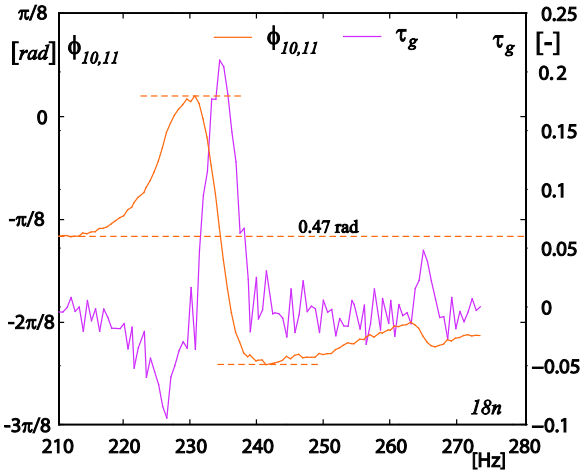

Fig. 15 Phase and group delay between guide vane o_{10} and o_{11} relative fluctuating bending displacement

6. Conclusions

One of the main excitation sources in hydraulic pump-turbines is the rotor-stator interaction due to impeller blade passage in the wake of guide vanes. The pressure fluctuations in the rotor-stator vaneless gap have generally been shown to increase linearly with the operating specific energy, subjecting the pump-turbines components to very high stresses at high head operations. However, the present study shows that the pressure fluctuations amplitude may strongly decrease close to guide vanes reaching resonance. The exciting frequencies at which the pressure fluctuations are minimal do not correspond to those at which the guide vanes exhibit maximum vibration amplitude; they are up to 5% higher. Guide vanes resonance is nonetheless at the origin of this phenomenon. The resulting phase shift between their vibrating motions may be the reason of the pressure fluctuation amplitude attenuation. The pressure fluctuations in the rotor-stator vaneless gap are minimal when the phase shift between guide vanes vibrations is the farthest from the phase shift, only due to the impeller blade passage, observed out of resonance.

Finally, the present paper gives rise to two main points. On the one hand, higher pressure fluctuations amplitude should not always be directly related to higher guide vanes vibrations amplitude. On the other hand, one could consider the guide vanes vibrations as an active control system to reduce the pressure fluctuations in the impeller of pump-turbines.

Acknowledgments

The present investigation was carried out in the frame of HYDRODYNA II project (Eureka N° 4150), in a partnership with ALSTOM Hydro, ANDRITZ Hydro, VOITH Hydro and UPC-CDIF. The authors would like to thank the Swiss Federal Commission for the Technology and Innovation (CTI) and Swisselectric Research for their financial support as well as the HYDRODYNA II partners for their involvement and support.

Nomenclature

$D_{\bar{1}e}$	Ref. diameter, impeller outlet ext. diameter [m]	p_k	k[th] modal component of flow pressure [Pa]
E	Specific energy [J/kg]	t	Time [s]
E_{exp}	Experimental value of specific energy [J/kg]	y_{oi}	Bending displacement [m]
F_{oi}	Bending force applied on i^{th} guide vane [N]	y'_{oi}	Relative fluctuating bending displacement [-]
M	Segmented time signal length [-]	$\bar{y}_{oi}$	Bending displacement time average [m]
M_t	Total time signal length [-]	$\widetilde{y'}_{oi}$	RMS-value y'_{oi} [-]
N	Impeller rotation speed [min^{-1}]	z_b	Impeller blades number [-]
$\overline{P_{y'y'}}(f)$	Power spectrum density of signal y' [-]	z_o	Guide vanes number [-]
$\overline{P_{c_pc_p}}(f)$	Power spectrum density of signal c_p [-]	α_o	Guide vanes opening angle [°]
Q	Discharge [m^3/s]	$\delta_{\varphi_{\bar{1}e}}$	Relative difference of discharge coefficient [-]
Q_{exp}	Experimental value of discharge [m^3/s]	$\delta_{\psi_{\bar{1}e}}$	Relative difference of energy coefficient [-]
$S_{1,oi}$	Volt. signal of first Wheatstone bridge [V]	$\phi_{10,11}$	Phase shift between $y'_{o_{10}}$ and $y'_{o_{11}}$ [rad]
$S_{2,oi}$	Volt. signal of second Wheatstone bridge [V]	ϕ_k	Phase of the pressure k[th] modal component [rad]
a_i	1[st] calibration coefficient [N/V]	$\varphi_{\bar{1}e}$	Pump-turbine discharge coefficient [-]
b_i	2[nd] calibration coefficient [N/V]	η	Pump-turbine efficiency [-]
c_i	Bending stiffness coefficient [N/m]	η_{max}	Pump-turbine maximum efficiency [-]
$c_{p,l}$	Pressure fluctuations factor of l^{th} sensor [-]	ν	Pump-turbine specific speed [-]
$\tilde{c}_{p,l}$	RMS-value of pressure fluctuations factor [-]	ρ	Fluid density [kg/m^3]
f	Frequency [Hz]	θ_{oi}	i^{th} guide vane angular position [°]
k	Number of diametrical nodes [rad^{-1}]	θ_s	Angular position in the stator [rad]
n	Impeller frequency [Hz]	$\psi_{\bar{1}e}$	Pump-turbine specific energy coefficient [-]
o_i	Guide vane position identifier ($1 \leq i \leq 20$)	τ_g	Negative of the phase shift change rate [rad.s]
p	Flow pressure [Pa]		

References

[1] Coutu A., Roy M. D., Monette Ch., Nennemann B., 2008, "*Experiments with Rotor-Stator Interaction in High Head Francis Turbine*". Proceeding of the IAHR 24th Symposium on Hydraulic Machinery and Systems. Foz Do Iguassu, Brazil.

[2] Fisher R.K., Seidel U., Grosse G., Gfeller W. and Klinger R. 2002."*A Case Study in Resonant Hydroelastic Vibration: The Causes of Runner Cracks and the Solutions Implemented for the Xiaolangdi Hydroelectric Project*". Proceedings of the 21st IAHR Symposium on Hydraulic Machinery and Systems, Lausanne, Switzerland.

[3] Potashnik P.I. 1979. "*Some Problems in Operation of the Kiev Pumped-Storage Station*". Power Technology and Engineering (Formerly Hydrotechnical Construction). Vol.12. No. 7. pp. 658-663.

[4] Nennemann, B. and Parkinson E., 2010, "*YiXing pump turbine guide vane vibrations: problem resolution with advanced CFD analysis*". 25th IAHR Symposium on Hydraulic Machinery and Systems. IOP Conf. Series: Earth and Environmental Science. Vol 12.

[5] Azevedo C.R.F, Magarotto D., Araújo J.A., Ferreira J.L.A. 2009. "*Bending fatigue of stainless steel shear pins belonging to a hydroelectric plant*". Engineering Failure Analysis. Vol.16. pp.1126-1140.

[6] Henscheid P.J. 2009. "*Sticky Wickets: In-Place Replacement of a Wicket Gate*". Hydro review. Vol. 28. No. 7.

[7] Tanaka, H. "*Vibration behavior and dynamic stress of runner of very high head reversible pump-turbine*". Proceeding of the 15th IAHR Symposium on Hydraulic Machinery and Systems. Belgrade, Serbia.

[8] Tanaka, H. "*Special design considerations for ultra high head pump-turbines*". The International Journal of Hydropower & Dams. November 1994.

[9] Zobeiri, A., Kueny, J. L., Farhat, M. and Avellan, F., 2006 "*Pump-Turbine Rotor-Stator Interactions in Generating Mode: Pressure fluctuation in Distributor Channel*". Proceedings of the 23th Symposium on Hydraulic Machinery and System, Yokohama, Japan.

[10] Roth, S., Hasmatuchi, V., Botero, F., Farhat M. and Avellan, F., 2010, "*Advanced Instrumentation for Measuring Fluid-Structure Coupling Phenomena in the Guide Vanes of a Pump-Turbine Scale Model*", Proceedings of the ASME 2010 7th International Symposium on Fluid-Structure Interactions, Flow-Sound Interactions, and Flow-Induced Vibration & Noise. Montreal, Canada.

[11] Roth, S., Hasmatuchi, V., Botero, F., Farhat M. and Avellan, F., 2010, "*Fluid-Structure Coupling in the Guide Vanes Cascade of a Pump-Turbine Scale Model*", Proceedings of the 25th IAHR Symposium on Hydraulic Machinery and Systems. Timisoara, Romania.

[12] International Electrotechnical Commission, 1999, "*Hydraulic Turbines, Storage Pumps and Pump-Turbines – Model Acceptance Tests*", International Standards IEC 60193, 2nd Edition.

[13] Farhat M., Natal S., Avellan F., Paquet F., Lowis PY., Couston M., 2002, "*Onboard Measurement of Pressure and Strain Fluctuations in a Model of Low Head Francis Turbine, Part1: Instrumentation*", Proceedings of the 21st Symposium on Hydraulic Machinery and System, Lausanne, Switzerland.

[14] Del Pedro M., Pahud P., 2003, "*Mécanique vibratoire, systèmes discrets linéaires*". Presses Polytechniques et Universitaires Romandes. Lausanne, Switzerland.